CORPUS PUBLISHERS

Journal of Mineral and Material Science (JMMS)

Volume 2 Issue 1, 2021

Article Information

Received date : July 18, 2020

Published date: January 21, 2021

*Corresponding author

Ashok P Tadamalle, Department of Mechanical Engineering, Sinhgad College of Engineering, Vadgaon (Bk), Pune, India

Keywords

Replace with Nd; YAG Laser; Weld Strength; Microstrain; Dislocation Density; Dissimilar Metals

Abbreviations

EDM: Electron Discharge Machine; UTS: Ultimate Tensile Strength; FIE: Fuel Instruments and Engineers; XRD: X-Ray Diffraction

Research Article

Analysis of Nd:YAG Laser Weld Thin Sheets of 304L and Galvanized Iron

Tadamalle AP*, Reddy YP and Kapatkar VN

Department of Mechanical Engineering, Sinhgad College of Engineering, India

Abstract

Nd:YAG Laser welding has been used for the joining of dissimilar metal Thin Sheets of 304L and Galvanized Iron Sheet in a but joint configuration. The laser weld joint provides better weld as compared to traditional welding methods, to obtain perfect butt-welding of thin dissimilar metals welds without defects relatively difficult. The experiments were conducted on 0.5 mm thin sheets to evaluate the weld joint characteristics. The experiments were conducted as per the Taguchi orthogonal array design matrix. Weld samples are tested on SEM and XRD for obtaining chemical composition and intercellular spacing at different detector positions. A change in chemical composition and strength of weld joints and also computed the grain size, microstrain, and dislocation density on weld top surface. The results of strength and weld bead dimensions obtained from the analytical method are in close agreement with each other. The outcome of the research work is useful for analyzing the weld top surface characteristics.

Introduction

In recent years, a new trend has been developed in industries for getting custom made properties by joining different materials. The utilization of laser technology to produce dissimilar material joint offers specific advantages in the welding of thin sheet metals. It is necessary to have the weld joint quality and its properties closer to the base metal properties. The weld joint quality and its performance are based on careful consideration of laser welding process parameters, process requirements, and the related process considerations. The critical performance parameters used for assessing dissimilar metal weld joint are weld quality, weld pool volume, microstructural and mechanical properties. The variation in properties and dimensions of heat affected zone significantly affects the performance parameters. In the molten weld pool, the heat and fluid flow have a significant influence on temperature gradient, cooling rates, and the solidification structure. The fluid flow and the convective heat transfer in the weld pool control the depth of penetration and shape of the fusion zone formation. The laser welding process has many advantages compared to the traditional joining process. In traditional weld joint quality is often influenced by the vacuum conditions. However, it has drawbacks such as high cost of equipment, maintenance, faster heating and cooling, and poor gap bridging [1,2]. The effect of process parameters on chemical composition, weld strength, and microhardness dissimilar metals of 0.5 mm is studied and factors responsible for the change in chemical composition, microhardness, and strength are presented. The welding experiments are carried out on 0.5 mm thickness dissimilar weld joints to investigate the effect of process parameters on a different type of weld joints [3,4]. The welding of 304 stainless steel sheets is examined for the prediction of melting efficiency. It was found that it depends on the fusion zone aspect ratio and melting efficiency initially increases and then slowly decreases. The evaluation of changes in microstructure and mechanical properties of Cu-Cr-Zr alloy and austenitic stainless steel welded using Laser welding and GTAW process. The study on change in microstructures, HAZ, and mechanical properties of dissimilar Nd:YAG laser lap welds of dissimilar metal is carried out and found that high cooling rates lead to an austenitic microstructure and axisymmetric fusion occurs. the dilution between two base metals strongly depends on the laser welding mode [5-8]. The sulfur and phosphorous impurities in the welding effect on dilution phenomenon. The effect of shielding gas on the microstructure and hardness of the weld zone is analyzed. The shielding gas affects the weld pool growth, diffusion of metals, microhardness, and microstructural changes [9,10].

The gap tolerance plays a significant role in the metallurgical and mechanical properties of weld joints. The formation of intermetallic brittle phases and weld defects are minimized by shifting a laser beam focus point towards Inconel. The ANSI 316 and ANSI 1008 metal weld joints reveal the presence of austenite and ferrite structure in fusion zone which increases the hardness The microscopic and X-ray radiography techniques are used to predict the amount of porosity in conduction mode welding [11-13]. A pseudo-binary diagram is used for the prediction of equilibrium microstructure constituents in stainless steel welds with the help of the modified Schaffler diagram. The ratio of chromium to nickel equivalent in the weld zone decides the formation of austenite and ferrite. The welding of ANSI 347 and 13CrMo44 steel joint microstructure contains both austenite and martensitic structure [14]. The keyhole formation and shielding gas have a significant effect on weld pool growth, a transition from conduction to the keyhole, diffusion of two metals, microhardness, and microstructure changes. The effect of Zn and Al coating on steel is analyzed for the formation of intermetallic phases and their effect on the thickness of the intermetallic reaction layer [15-17]. The present work focuses on understanding the physical phenomenon involved in laser welding of micro components made of dissimilar metals. The effect of weld process parameters on weld bead dimensions, strength, grain size, the chemical composition of dissimilar weld joints was discussed.

Material and Procedure

The schematic diagram of the experimental setup used for experimentation is shown in Figure 1 and the range and level of process parameters are given in Table1. Samples were welded as per Taguchi's L8 matrix using Trumpf make, True Laser Station 5004, pulsed Nd: YAG laser welding machine designed to deliver up to 4 kW of laser power. The range of process parameters used for experimentation was selected by taking several trail experiments. The weld specimens of size 150 mm×60 mm are cut using wire cut electron discharge machine. Before welding, the workpiece samples are decreased and cleaned using a 6-8 % NaOH solution and followed by a 15-20 % HNO_3 solution.

Table 1: Chemical composition, Process parameters and their levels.

Parameters	Unit	Values	Parameters	Unit	Values	Parameters	Unit	Values
Laser power	W	1500-1700	Wavelength	µm	1064	Focal distance	mm	150
Welding Speed	mm/s	4-5	Beam Angle	θ	90±1	Ar Gas flow rate	lpm	7
Pulse duration	ms	2-Jan	Gap	mm	0.01	Beam diameter	mm	0.8
Elements	**%C**	**%Mn**	**%Si**	**%Ni**	**%Cr**	**%Mo**	**%S**	**%P**
304L SS	0.03	1.09	0.38	0.03	17.9	8.99	0.66	0.45
GI	0.06	0.4	0.02	0.01	0.01	0.03	0.001	0.05

Figure 1: Experimental setup, fixture and samples

The chemical and physical properties of dissimilar weld joint changes when it is subjected to a high-temperature gradient. The chemical composition of 304L Stainless Steel and Galvanized Iron sheets coated with 7 µm thick zinc layer is obtained by using Spectro make, optical emission spectrometer (SPECTROMAXx) is given in Table 2. A piece of 6 mm to 8 mm is cut from the welded region by using Wire Electron Discharge Machine (EDM) for metallographic analysis. The samples were polished using 120-800 emery grits, followed by Leco DP-red oil-based lubricant and finally a slurry of alumina and diamond with 9-1 µm to produce a scratch-free and mirror finish. Then the samples are etched with 4% Nital, and 20 ml HCl, 1.0 g sodium meta bisulfate, and water. Also, 10 % of oxalic acid is used to reveal weld joint features.

Weld Bead Dimensions and Tensile Strength

The weld bead geometry is an important characteristic of the weld joint and plays a major role in weldment as it affects the performance of the weld joint. The microstructure images of the weld joint captured using an eye-piece lens (16X) and objective lens (50X) magnification. The depth of penetration is estimated using an analytical equation developed based on the sheet thickness and material properties. The Ultimate Tensile Strength (UTS) and Microhardness are essential mechanical properties to understand the behavior of materials. The tensile test specimens are cut by using water jet machining from weld plates as per the ASTM E8 standard. The results obtained from UTS for a different combination of process parameters. The cut specimens are tested for strength on Fuel Instruments and Engineers (FIE) make, Model-UTN-40, Capacity 400 kN, Universal Tensile Testing Machine. The sets of weld bead geometry dimensions are measured from each sample using image analyzer and strength were given in Table 2.

Weld Top Surface Point Scans

The weld bead top surface analysis has been carried out using SEM to understand the variation in the chemical composition of the surface exposed to the atmosphere is obtained is presented in Figure 2. The results of weight percentage of O, Si, Cr, Mn, Fe, and Ni obtained from weld pool regions using XRD. The distribution of alloying elements over the weld pool top surface is presented in Table 3. The change in chemical composition and formation of different constituents during solidification of the weld pool top surfaces are analyzed.

The characterization of microstructure, phase, and chemical composition is analyzed using X-Ray Diffraction(XRD) techniques. The FM-ARS 9000, Philips PAN_Analytical, High-speed X-Ray Diffractometer which is used for the measurement of the distance between crystal planes are tabulated in Table 4 and corresponding XRD scan patterns are given in Figure 3. These patterns are mapped in a single frame to study the peak patterns. The peak locations are considered for computing dislocation density, grain size, and microstrain in the weld joint using the equation proposed [14].

Table 2: Bead dimensions, Ultimate tensile strength and Fracture position.

Experiment Number	Input Variables			Responses			
	P (W)	v (mm/s)	PD (ms)	BW (µm)	DOP (µm)	UTS (N/mm²)	Fracture position
1	1500	4.0	1.0	836	154	69.89	Weld seam
2	1500	4.0	2.0	875	237	112.6	Weld seam
3	1500	5.0	1.0	830	293	115.33	Weld seam
4	1500	5.0	2.0	867	339	203.45	Weld seam
5	1700	4.0	1.0	830	255	234.13	Weld seam
6	1700	4.0	2.0	1022	519	285.4	G.I. base metal
7	1700	5.0	1.0	888	387	228.48	Weld seam
8	1700	5.0	2.0	931	459	257.88	G.I. base metal

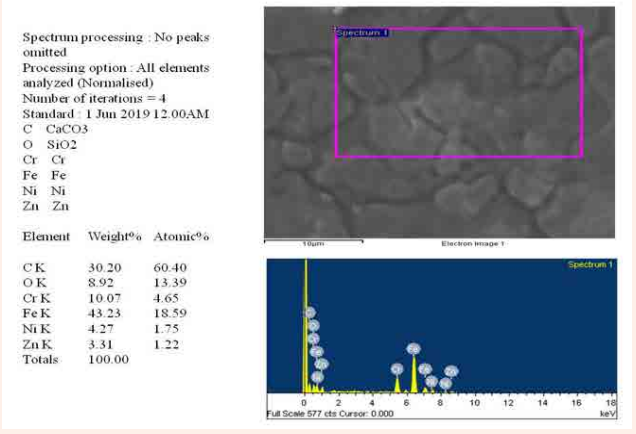

Figure 2: Typical SEM results of Experiment Number 5.

Table 3: Chemical composition of weld pool top surface.

Experiment number	Weld zone constituents						Dominating factor
	C	O	Cr	Fe	Ni	Zn	
1	16.59	9.56	13.39	50.2	5.3	4.96	Ferric Oxide
2	26.73	--	11.91	52.18	6.68	2.51	Ferric Oxide
3	27.74	--	13.06	51.17	6.55	1.49	Ferric Oxide
4	17.03	21.42	0.71	2.61	--	58.23	Zinc Oxide
5	30.2	8.92	10.07	43.23	4.27	3.31	Ferric Oxide
6	19.6	8.3	12.4	50.33	5.93	3.44	Ferric Oxide
7	18.67	9.05	11.68	49.25	4.75	2.01	Ferric Oxide
8	21.35	8.95	12.89	46.14	6.24	1.83	Ferric Oxide

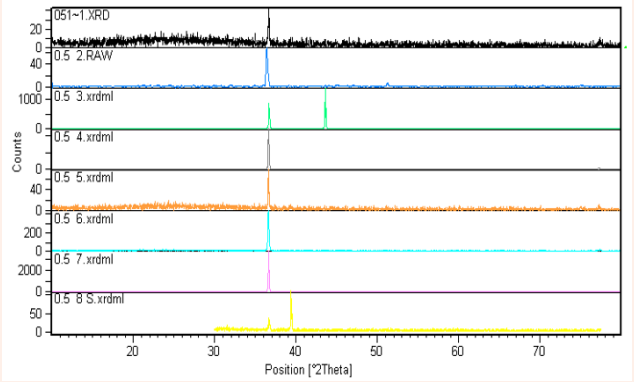

Figure 3: XRD Peaks obtained from 0.5 mm weld joints.

Table 4: XRD peak position results of weld joints.

Numbers	Position [°2θx]	Height [cts]	FWHM [°2θx]	d-spacing [Å]
1	36.6964	31.24	0.1968	2.44904
2	36.4506	66.98	0.264	2.46295
3	43.6266	1337.42	0.072	2.07302
4	36.6597	2340.91	0.12	2.44938
5	36.6528	44.1	0.24	2.44983
6	36.6563	360.01	0.2165	2.45163
7	36.6645	3704.78	0.072	2.44907
8	39.4448	52.91	0.24	2.28262

Results and Discussion

In this section, the effect of process parameters on depth of penetration, weld defects, strength, microhardness, grain size, chemical composition, phase contents, and microstructure are discussed. The focused high energy density laser heat source on weld material produces a narrow heat-affected zone and weld geometry obtained from the optical microscope is shown in Figure 4. The darker portion of the weld joint represents galvanized iron, the brighter portion belongs to stainless steel, whereas the middle portion represents the weld pool region. The observation reveals that the uneven melting of the weld pool region occurred on either side. The higher melting is observed towards the GI side than the 304L SS side. This is due to a difference in thermal diffusivity of metals. The weld samples prepared at a laser power of 1500 W reveal partial penetration, porosity, and improper mixing, whereas samples welded at 1700 W shows the better depth of penetration, proper mixing, and no porosity except in the samples welded at 1 ms pulse duration. Full-depth of penetration is reported from the experimental results at 2 ms pulse duration and a laser power of 1700 W irrespective of welding speed.

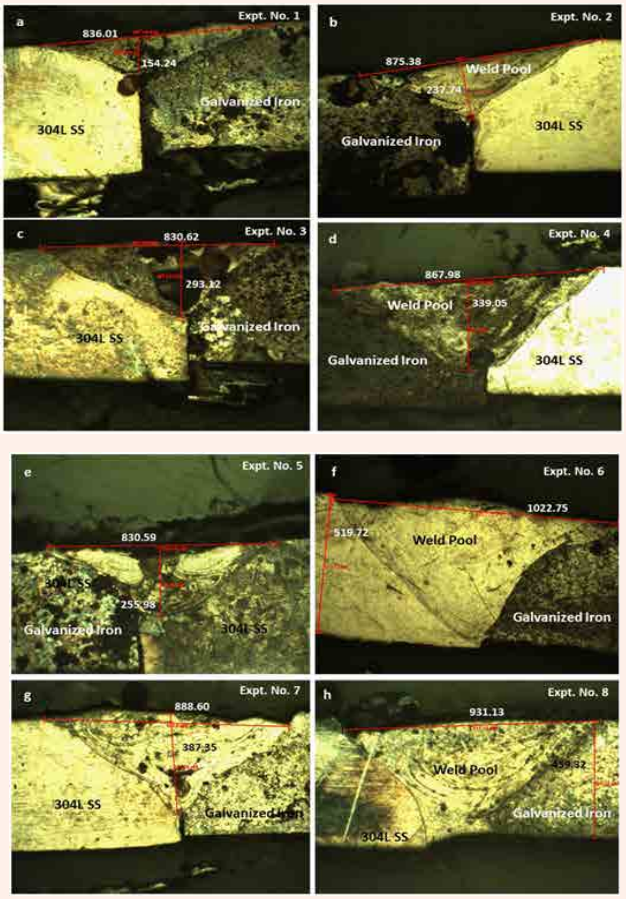

Figure 4: Weld bead geometry and dimensions.

The micrographs depict that the combined process parameters have a significant effect on weld bead geometry rather than a single process parameter. The DOP computed using an analytical equation [18] and the experimentally are given in Figure 5. The DOP estimated using the analytical method for the galvanized iron sheet is found to be greater than 304L stainless steel. The measured experimental and analytical results are found to be in close agreement in the majority of the experiments. The average DOP both metals is considered for experimental validation by assuming an equal amount of melting occurred in both metals.

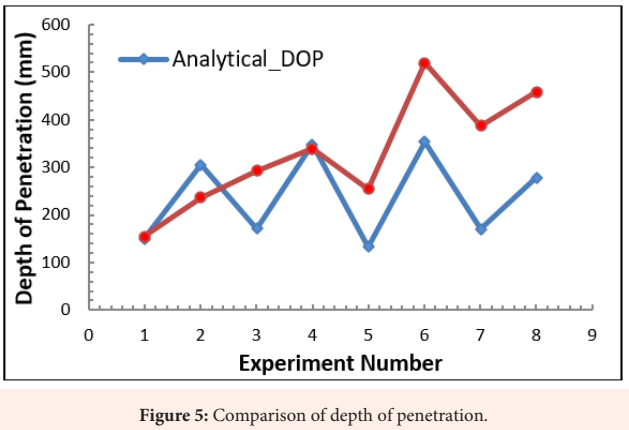

Figure 5: Comparison of depth of penetration.

The weld samples prepared for tensile testing as per ASTM E8 and the results obtained are presented in Figure 6. The experiment number 6 reveals the highest strength of 285.4 N/mm^2 as it is welded at a laser power of 1700 W whereas experiment number 8 has moderate strength of 257.88 N/mm^2 and samples welded at a laser power of 1500 W have strength ranging from 69.89 N/mm^2 to 203.45 N/mm^2 all other samples have strength less than 234.13 N/mm^2. A lower strength is reported in the welds fabricated at 1500 W laser power, 5 mm/s welding speed, and 1 ms pulse duration. The weld samples found to be failed in the weld seam zone for experiment numbers 1 to 5 and 7 whereas experiment numbers 6 and 8 failed in the galvanized iron base metal. The failure in the weld seam zone is due to weld defects and insufficient depth of penetration, whereas the failure in galvanized iron base metal is due to the full depth of penetration which results in better weld strength than galvanized iron. The microhardness result reveals that 279 to 376 VHN and 240 to 352 VHN in parallel and perpendicular to the weld top surface respectively [4] and it is in line with the tensile strength results.

The presence of different elements and corresponding weight percentages of O, Si, Cr, Mn, Fe, and Ni obtained from the weld pool region and base metals are given in Table 5. The elements in the weld pool region are found to be significantly varied as compared to the base metal composition. The uneven distribution of chemical composition leads to solute element deviation from its average composition. This is due to insufficient time to react with the elements, vaporization of alloying elements, a rapid cooling rate which results in unbalanced crystallization, phase transition, and diffusion of alloying elements. The experiment number 4 shows the formation of zinc oxides at the faying surface of the welds. The reporting of the zinc oxide on the weld pool top surface depends on the selection of sample locations considered for the study. If the sample readings are taken either at the start or end of the weld, more amount of zinc deposition is observed and the middle portion of the weld small amount zinc contents is found as the zinc vaporizes at lower temperatures than base metals. The XRD peaks obtained from all weld samples correspond to the formation of austenite, δ-ferrite, and carbides. The chromium to nickel ratio is found to be 1.09 which is less than 1.5. It reveals the presence of austenitic constituents [3].

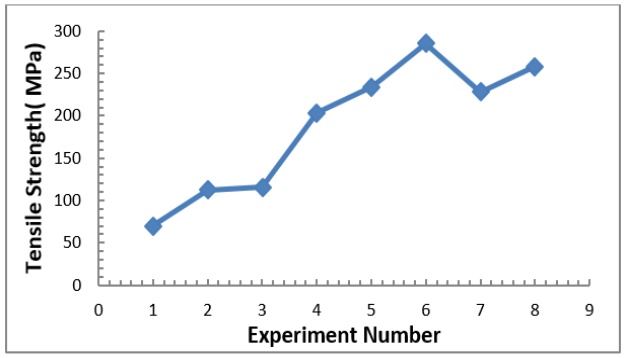

Figure 6: Tensile strength obtained at different process parameters.

Table 5: Variation of chemical composition.

Element	Average variation in Fusion Zone	Base Metal Weight %		% Variation	
		304L SS	GI	304L SS	GI
O	0.012	0.01	4.97	16.67	99.73
Si	0.335	0.45	0.02	25.6	94.03
Cr	11.97	18.68	0.01	35.88	99.91
Mn	1.07	2.08	0.4	48.66	62.61
Fe	81.35	69.63	95.03	15.43	14.39
Ni	5.25	9.16	0.01	42.68	99.81

The weld strength depends on the grain size pattern and configuration of the thermal cycle during the welding process. The peak locations were considered for estimation of dislocation density, grain size, and microstrain in welds using equation [14]. The (Figures 7 & 8) reveals the relationship between process parameters and grain size, dislocation density, and microstrain. It is observed that greater grain size in sample numbers 3 and 7, whereas an opposite tendency, is observed for the dislocation density and microstrain. The average grain size, dislocation density, and microstrain estimated at peak intensities are 17.69 µm, 0.005 kg/mm^3, and 0.037 respectively. The maximum and minimum grain size of 26 readings (average) is 0.072 µm and 0.0001 µm respectively. The reason for getting higher hardness and strength is due to the formation of coarse grains and solidified dendrite structure of austenite and ferrite.

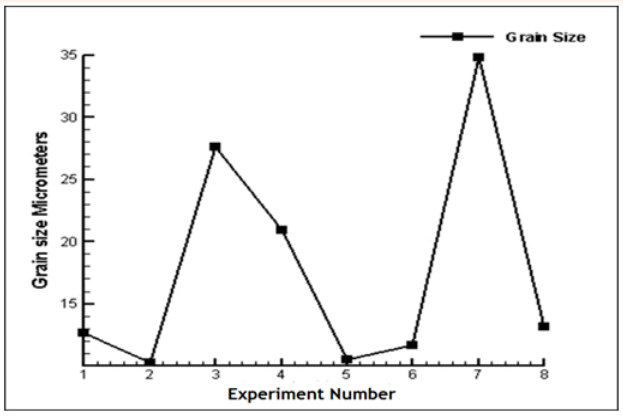

Figure 7: Variation of grain size.

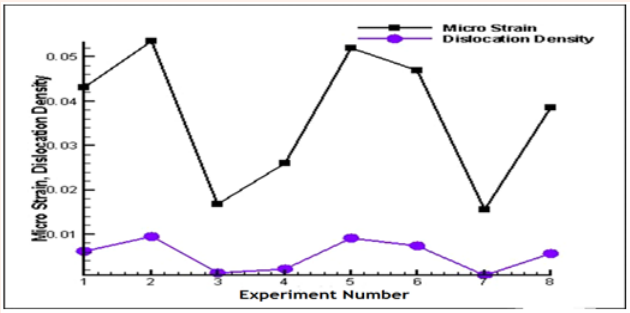

Figure 8: Variation of micro strain and dislocation density.

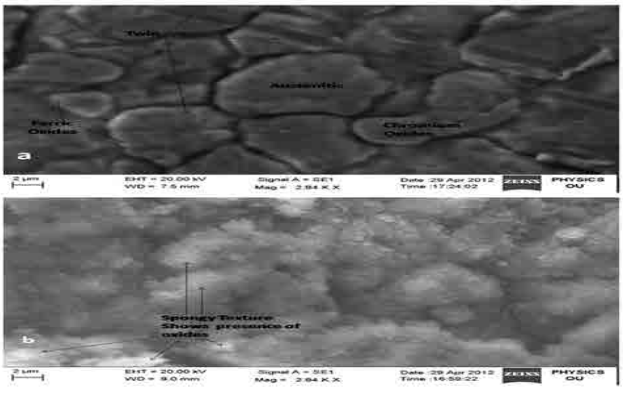

Figure 9: Micrographs of weld top surface at different magnifications.

The analysis of Figure 9 depicts the presence of δ-ferrite traces in the weldment region near the weld interface line. A solidified weld pool discloses the formation of SiO_2, FeO_3, and oxide inclusion were evenly distributed across the weld pool region. The Pebble like iron oxides in the welds is realized in the form of safe and broken bubbles after etching. The maximum size of the bubble formed in the weld region is around 15 µm in diameter. This is due to the trapping of zinc oxides during solidification. The enrichment of chromium and nickel constituents is also found adjacent to the weld interface region.

Conclusion

The laser welding of 304L SS and GI sheets of 0.5 mm thickness was carried out to understand the phenomenon involved in the welding of dissimilar metal. Experiments are conducted as per the Taguchi's orthogonal array design matrix. The weld joints are examined and tested for, strength and analyzed for the changes in microstructures, porosity, weld bead geometry, change in chemical composition, phase contents using SEM, whereas microstrain, dislocation density, and grain size are determined using the obtained from XRD. A better weld strength of 285.4 N/mm^2 is reported in welds created at a laser power of 1700 W whereas, 203.45 N/mm^2 strength is reported at a laser power of 1500 W. The C_{req}/N_{ieq} ratio reveals the phase transition to austenite and 2-3% volume of ferrite. The weight percentage of O, Si, Cr, Mn, Fe, and Ni is found to be significantly varied in the weld pool region as compared to the base metals. The chemical quantification analysis obtained from the line scan reveals 81.35 weight % of iron and 11.97 weight % of chromium variation in the weld pool region. The maximum size of a bubble formed in the weld region is around 15 μm in diameter

References

1. Benyounis KY, Olabi AG, Hashmi MSJ (2005) Optimizing the laser-welded butt joints of medium carbon steel using RSM. Journal of Materials Processing Technology 164: 986-989.
2. Junjie M, Masoud H, Blair C, Radovan K (2014) Dissimilar joining of galvanized high-strength steel to aluminum alloy in a zero-gap lap joint configuration by two-pass laser welding. Materials and Design 58: 390-401.
3. Tadamalle AP, Reddy YP, Ramjee E, Reddy VK (2017) Characterization of fully and partially penetrated Nd: YAG laser weld dissimilar metal joints. Journal of Mechanical Sciences and Technology 32: 615-621.
4. Tadamalle AP, Reddy YP, Ramjee E, Reddy VK (2016) Characterization of stainless steel and galvanized iron 0.5 mm thick laser weld joints. International Journal of Advanced Manufacturing Technology 90: 383-395.
5. Fuerschbach PW, Eisler GR (1999) Effect of very high travel speed on melting efficiency in laser beam welding. SAE International Journal of Materials and Manufacturing 108: 824-829.
6. Chang CC, Wu LH, Shueh C, Chan CK, Shen IC, et al. (2016) Evaluation of microstructure and mechanical properties of dissimilar welding of copper alloy and stainless steel. Int J Adv Manuf Technol 91: 2217-2224.
7. Sufizadeh AR, Mousavi SA (2017) Microstructures and mechanical properties of dissimilar Nd:YAG laser weldments of AISI4340 and AISI316L steels. International Journal of Minerals, Metallurgy and Materials 24: 538- 549.
8. Torkamany MJ, Sabbaghzadeh J, Hamedi MJ (2012) Effect of laser welding mode on microstructure and mechanical performance of dissimilar laser spot welds between low carbon steels and austenitic stainless steels. Materials and Design 34: 666-672.
9. Springer H, Szczepaniak A, Raabe D (2015) On the role of zinc on the formation and growth of intermetallic phases during inter diffusion between steel and aluminium alloys. Acta Materialia 96: 203-211.
10. Zhang WP, Li SX, Zhang ZF (2011) General relationship between strength and hardness. Materials Science and Engineering-A 529: 62-73.
11. Ming LZ, Fu ZX (2010) Correlation between microstructure, hardness and strength in HAZ of dissimilar welds of rotor steels. Materials Science and Engineering- A 527: 4035-4042.
12. Long C, Longzao Z, Chao T, Wei H, Chunming W, et al. (2014) Study of laser butt welding of SUS301L stainless steel and welding joint analysis. International Journal of Advanced Manufacturing Technology 73: 1695-1704.
13. Sathiya P, Mahendar KM, Shanmugarajan B (2012) Effect of shielding gases on microstructure and mechanical properties of super austenitic stainless steel by hybrid welding. Materials and Design 33: 203-212.
14. Ahmad M, Mohammad RF, Mohammad RM (2012) Modified Scherrer Equation to estimate more accurately nano-crystallite size using XRD. World Journal of Nano-Science and Engineering 2: 154-160.
15. Szczepaniak A, Jianfeng F, Aleksander K, Dierk R (2012) On the correlation between thermal cycle and formation of intermetallic phases at the interface of laser-welded aluminum-steel overlap joints. Advanced Engineering Material 14: 1-7.
16. Wang P, Lu SP, Xiao NM, Li DZ, Li YY (2010) Effect of delta ferrite on impact properties of low carbon 13Cr-4Ni Martensitic stainless steel. Material Science and Engineering-A 527: 3210-3216.
17. Suutala N, Takola T, Moisio T (1979) Singlre phase ferritic solidification mode in austenitic ferritic stainless steel welds. Metallurgical Transactions A 10: 1183-1190.
18. Ikhwan NN, Jalil AM, Fadhali P, Yupapin P (2012) Nd: YAG laser welding for photonics devices packaging. pp. 1-18.